



Inverted-V Electron Acceleration Events Concurring With Localized Auroral Observations at Mars by MAVEN

Shaosui Xu, David L. Mitchell, James P. Mcfadden, Matthew O. Fillingim, Laila Andersson, David A. Brain, Tristan Weber, Nicholas M. Schneider, Sonal Jain, Christopher M. Fowler, et al.

► To cite this version:

Shaosui Xu, David L. Mitchell, James P. Mcfadden, Matthew O. Fillingim, Laila Andersson, et al.. Inverted-V Electron Acceleration Events Concurring With Localized Auroral Observations at Mars by MAVEN. *Geophysical Research Letters*, 2020, 47, 10.1029/2020GL087414 . insu-03673149

HAL Id: insu-03673149

<https://insu.hal.science/insu-03673149>

Submitted on 20 May 2022

HAL is a multi-disciplinary open access archive for the deposit and dissemination of scientific research documents, whether they are published or not. The documents may come from teaching and research institutions in France or abroad, or from public or private research centers.

Copyright

L'archive ouverte pluridisciplinaire **HAL**, est destinée au dépôt et à la diffusion de documents scientifiques de niveau recherche, publiés ou non, émanant des établissements d'enseignement et de recherche français ou étrangers, des laboratoires publics ou privés.

Geophysical Research Letters

RESEARCH LETTER

10.1029/2020GL087414

Key Points:

- We estimate a field-aligned potential drop of 440 V during an inverted-V electron acceleration event concurring with auroral observations
- The current density estimated from the observed magnetic perturbation reaches $1.1 \mu\text{A}/\text{m}^2$, agreeing with estimated net electron current
- Similar to Earth, this potential drop develops when the ambient plasma is unable to support the necessary field-aligned current

Supporting Information:

- Figure S1

Correspondence to:

S. Xu,
 shaosui.xu@ssl.berkeley.edu

Citation:

Xu, S., Mitchell, D. L., McFadden, J. P., Fillingim, M. O., Andersson, L., Brain, D. A., et al. (2020), Inverted-V electron acceleration events concurring with localized auroral observations at Mars by MAVEN. *Geophysical Research Letters*, 47, e2020GL087414. <https://doi.org/10.1029/2020GL087414>

Received 5 FEB 2020

Accepted 26 MAR 2020

Accepted article online 9 APR 2020

Inverted-V Electron Acceleration Events Concurring With Localized Auroral Observations at Mars by MAVEN

Shaosui Xu¹ , David L. Mitchell¹ , James P. McFadden¹, Matthew O. Fillingim¹ , Laila Andersson² , David A. Brain² , Tristan Weber² , Nicholas M. Schneider² , Sonal Jain² , Christopher M. Fowler² , Robert Lillis¹ , Christian Mazelle³ , and Jared Espley⁴ 

¹Space Sciences Laboratory, University of California, Berkeley, CA, USA, ²Laboratory for Atmospheric and Space Physics, University of Colorado Boulder, Boulder, CO, USA, ³IRAP, CNRS-University of Toulouse-UPS-CNRS, Toulouse, France, ⁴Goddard Space Flight Center, Greenbelt, MD, USA

Abstract From February to March 2019, the Mars Atmosphere and Volatile Evolution (MAVEN) spacecraft repeatedly observed aurora near periapsis over Mars' southern strong crustal fields. During these orbits, the Solar Wind Electron Analyzer observed accelerated electrons at similar locations to where the auroras were observed, resembling the inverted-V structure observed near Earth's auroral region. In this study, we present a case study of such an acceleration event, where we estimate a field-aligned electrostatic potential drop of ~ 440 V. We determine the field-aligned current from the observed magnetic perturbation reaches $1.1 \mu\text{A}/\text{m}^2$, agreeing reasonably well with the estimated net electron current carried by acceleration electrons with a maximum of $2.5 \mu\text{A}/\text{m}^2$. Similar to Earth, the potential drop develops when the ambient plasma cannot sustain the imposed field-aligned current. We also estimate the potential layer to be located above 750- to 850-km altitude and the associated electric field to be $\sim 0.6 \text{ V/m}$.

1. Introduction

Inverted-V electron acceleration events, characterized by an enhanced flux in a narrow energy band, have long been observed at Earth and are responsible for discrete auroral emissions (e.g., Birn et al., 2012; McFadden et al., 1986). These electrons are accelerated above the observational locations by a parallel electric field ($E_{||}$) within a narrow potential layer (typically a few kilometers in thickness) (e.g., Birn et al., 2012; Paschmann et al., 2002), attributed to one or more double layers in the auroral cavity (e.g., Ergun et al., 2004). The energy shifts are interpreted as the spacecraft passing below a time stationary potential structure with a “U” shape (the simplest structure), an “S” shape, or more complicated shapes (see example schematics in our Figure 3 or in Marklund et al., 2007). The potentials associated with U shapes do not reach down to the atmosphere, while some or all of those associated with S shapes do. The inverted-V signature is a result of the spatial distribution of these potential structures and thus to be observed below these structures. Inverted-V electron signatures have been observed by a few spacecraft, for example, Freja (e.g., Haerendel et al., 1994) and the Fast Auroral Snapshot (FAST) mission (e.g., Partamies et al., 2008), and the potential drop tends to be located above Freja's orbit at $\sim 1,700$ km. However, the shape and altitude distribution of potential structures vary significantly depending on the boundary conditions. At Earth, the formation of this potential drop is associated with a shear in the magnetic field at the open-closed field line boundary or a twist in the magnetic field, indicating a field-aligned current. When this current cannot be sustained by ambient plasma, a parallel electric field is needed. At Jupiter, inverted-V electron acceleration events were also observed by Juno but were not the dominant source of the intense auroral emission, even though the acceleration is an order of magnitude more intense than at Earth (Mauk et al., 2017).

At Mars, the discovery of aurora was reported by Bertaux et al. (2005) using images from the Spectroscopy for Investigation of Characteristics of the Atmosphere of Mars (SPICAM) onboard Mars Express (MEx). Leblanc et al. (2006) and Liemohn et al. (2007) suggest that low-energy electrons peaking at 20–30 eV (i.e., unaccelerated solar wind electrons or ionospheric photoelectrons) might be responsible for emissions observed by SPICAM. Brain et al. (2006) reported inverted-V electron acceleration events with measurements from

the Mars Global Surveyor (MGS) spacecraft, where sharp spectral peaks were observed from 100 eV to 2.5 keV, and preferentially near the Martian crustal magnetic fields. For one orbit example in Brain et al. (2006), abrupt changes in magnetic field were observed at the edges of the inverted-V structure, indicative of field-aligned currents, which means the quasistatic electron acceleration was occurring similar to what often is associated with the inverted-V events observed at Earth. However, no UV observations that could have coincidentally identified aurora were made. Later, simultaneous auroral emission and accelerated electrons were observed by MEx, as reported by Leblanc et al. (2008). MEx also observed counterstreaming accelerated ions and electrons, indicative of an acceleration by a large-scale potential structure (Lundin et al., 2007). However, the lack of magnetic field measurements made it difficult to determine the acceleration process. In addition, it is worth mentioning that other types of auroras, triggered by other particle sources, are observed at Mars, including auroras produced by the solar energetic particles (SEP) electrons (Schneider et al., 2015, 2018) and auroras by solar wind proton precipitation (Deighan et al., 2018; Ritter et al., 2018).

During late February to early March 2019, the Imaging Ultraviolet Spectrograph (IUVS) instrument (McClintock et al., 2015) onboard MAVEN (Jakosky et al., 2015) repeatedly observed localized auroral emissions near periapsis over the southern strong crustal field region at Mars. During these orbits, the Solar Wind Electron Analyzer (SWEA) instrument (Mitchell et al., 2016) observed accelerated electrons at similar locations. In addition, magnetic vector field measurements from the magnetometer (MAG) instrument (Connerney et al., 2015) identified disturbances in the magnetic field suggesting field-aligned currents associated with the accelerated electrons. In this study, we utilize data from SWEA and MAG onboard MAVEN to investigate the mechanism for the observed electron acceleration with an event on 26 February 2019.

2. MAVEN Observations

Observations from MAVEN on 26 February 2019 are displayed in Figure 1, when the spacecraft passed through a region of strong crustal magnetic fields (geographic latitude from -58° to 15° and longitude from 163° to 189°) near periapsis and in the darkness (solar zenith angle $97\text{--}144^{\circ}$). Superthermal electron voids (electron fluxes close to the instrument background flux level) were observed for several time intervals in Figure 1a4, indicating closed crustal magnetic field loops, a common topology in this region (e.g., Steckiewicz et al., 2015, 2017). Between these voids, electron flux spikes are seen with one-sided loss cones (Figures 1a3 and 1b5), generally interpreted as electron precipitation along open-field lines in the cusps (e.g., Brain et al., 2007; Lillis & Brain, 2013; Weber et al., 2017, 2019; Xu et al., 2017).

From 11:05:50 universal time (UT) to 11:06:50 UT, the pitch angle (PA)-averaged electron energy spectra from SWEA (Figure 1b6) exhibit an organized signature in time, high electron fluxes concentrated in a narrow energy range with decreasing peak energies from ~ 500 to ~ 40 eV and then increasing peak energies back to ~ 500 eV. The descending and ascending peak energies resemble the inverted-V structures at Earth, and each spectral shape is similar to localized electron acceleration at Earth (Evans, 1974). We therefore interpret these data as the spacecraft passing in and out of magnetic field lines that have a field-aligned potential structure above the spacecraft. A more detailed analysis is presented in section 3.

In Figure 1b2, we show the variation (ΔB) for each magnetic vector component by subtracting two adjacent 1-s magnetic vector measurements, that is, $\Delta B = B_t - B_{t-1}$ for time-ordered data at a 1-s or 4-km cadence, which means we filter out variations less than 1 s. The smooth, systematic variation of the magnetic field over timescales of ~ 1 min (~ 240 km) results from passing through the large-scale magnetic field originating from crustal sources below the spacecraft. Small-scale and more abrupt perturbations in magnetic field are seen during 11:05:45–11:05:55 UT and 11:06:35–11:07:00 UT, right at the edges of the accelerated electron structure, indicative of a field-aligned current.

3. Field-Aligned Potential Estimation

To confirm that the observed energetic electrons are accelerated by field-aligned potentials, we examine whether the phase space densities are similar in shape to each other but shifted in energy, as illustrated in Figure 2. Here, phase space densities are obtained by averaging over PAs $0\text{--}60^{\circ}$ to account for downward electrons only, as the magnetic field points radially inward (Figure 1b1), which are mostly absorbed and form loss cone PAs $120\text{--}180^{\circ}$ (as shown in Figure 1b5). A few observations can be made. (1) The phase space density of the accelerated (blue) spectra remains roughly constant from a low energy ($\sim 25\text{--}60$ eV) to some higher energy (E_0) and then drops exponentially with increasing energy. This flat-top shape is interpreted

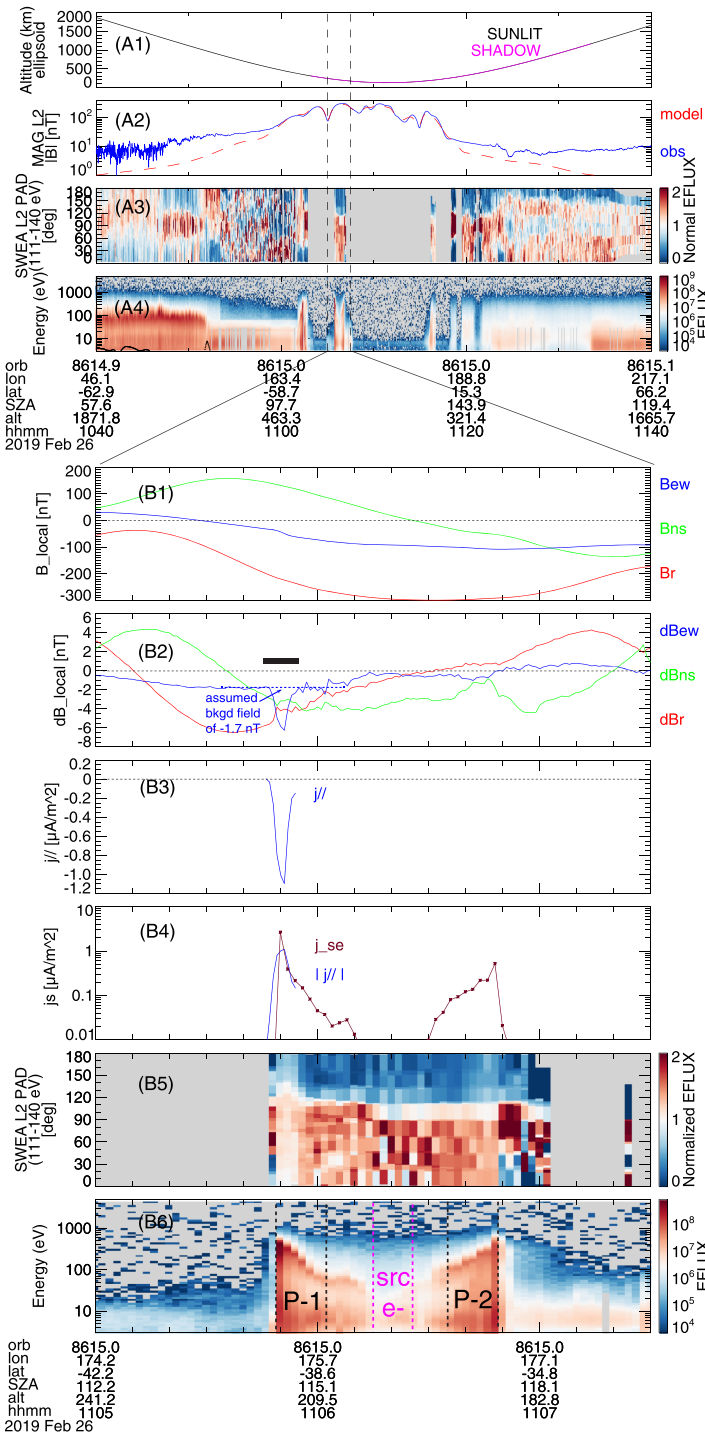


Figure 1. Time series on 26 February 2019 of (a1) MAVEN altitudes, (a2) observed (MAG, blue) and modeled (Morschhauser et al., 2014) (red) magnetic field magnitudes, normalized pitch angle distribution for 111–140 eV (a3) and averaged electron energy spectra (a4) measured by SWEA. Panels (b1)–(b6) show the zoom-in orbit: (b1) magnetic vectors (nT) relative to the local geographic plane (blue for the local east direction, green for the local north direction, and red for the radial direction), (b2) ΔB (nT) for each magnetic vector component (i.e., $\Delta B = B_t - B_{t-1}$ for time-ordered data at a 1-s or 4-km cadence), (b3) field-aligned current density (A/m^2) estimated from magnetic field measurements, (b4) the absolute parallel current density from ΔB (blue) and the net electron current carried by superthermal electrons (red), (b5) normalized pitch angle distribution for 111–140 eV, and (b6) pitch angle-averaged electron energy spectra measured by SWEA. Electron spectra within vertical dashed lines in panel (b6) are plotted in Figure 2. The gray vertical stripes below 30 eV in (a4), for example, 10:50–11:00 and 11:25–11:40 UT, identify data affected by sporadic low-energy electron suppression, an instrumental effect that occurred from January to April 2019 and is well understood.

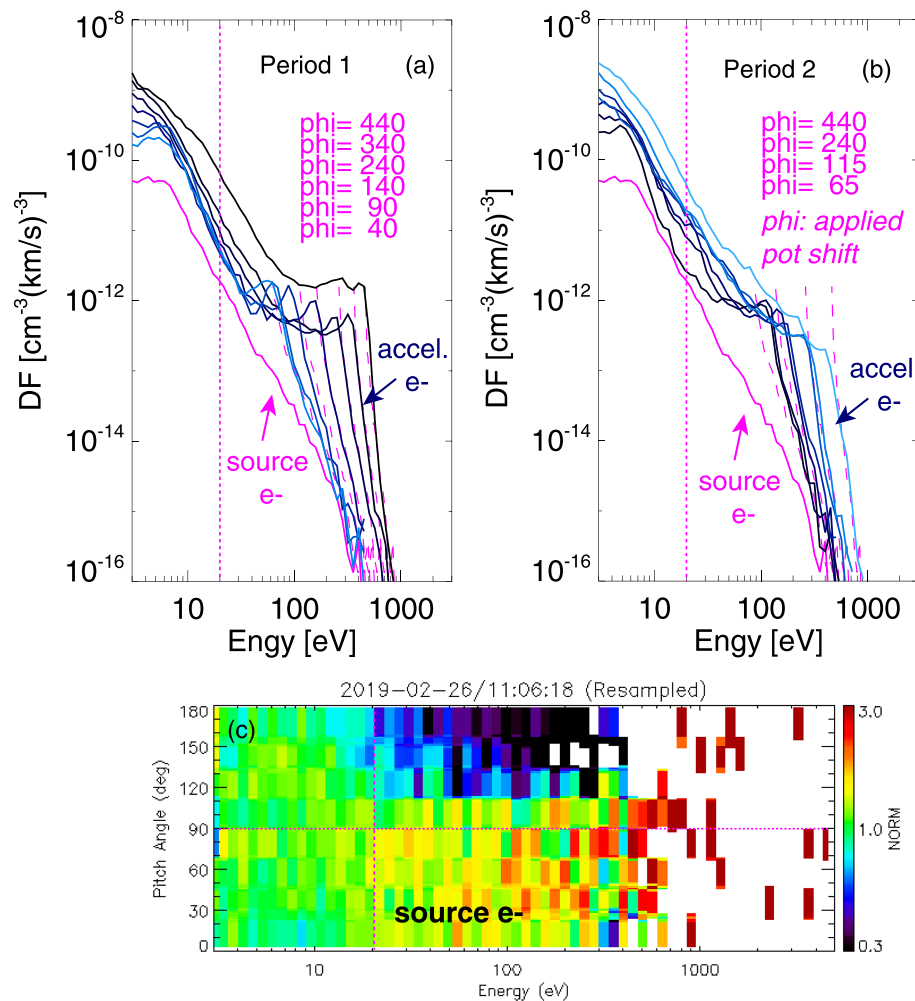


Figure 2. Electron distribution functions (DF) averaging over pitch angles $0\text{--}60^\circ$ (downward traveling) for the two time periods marked by vertical black lines in Figure 1b6, (a) for Period 1 (11:05:48–11:06:05 UT) and (b) for Period 2 (11:06:28–11:06:48 UT), colored in light (earlier times) to dark (later times) blue. The solid magenta lines are the assumed source electron DF to be compared with, averaging over a time range marked by the two vertical magenta lines in Figure 1b6. The dashed magenta lines are the source electron DF (only >20 eV used) shifted by some potentials (ϕ , labeled in the upper left corners). (c) The normalized pitch angle distribution for each energy, resampled into $128 \times 1.4^\circ$ bins, for source electrons.

as electrons being accelerated by an electrostatic potential, with a magnitude comparable to E_0 , similar to electrons in the sheath being accelerated by the cross-shock potential (e.g., Feldman et al., 1983; Schwartz et al., 2019). Some departures from the flat-top shape may be caused by a cold plasma beam (probably the local plasma at the potential layer) also accelerated by this potential drop (Akbari et al., 2019). (2) The high fluxes at low energies ($<\sim 25$ eV) are probably from a combination of secondary electrons created by impact ionization as these energetic beams interact with the neutral atmosphere below the spacecraft and also secondary electrons produced within the instrument by these beams. (3) The maximum acceleration is ~ 300 eV higher than what is observed in the sheath (not shown) so that these electrons cannot be simply precipitating sheath electron, but an acceleration mechanism is required, implying a field-aligned potential.

We can infer field-aligned potentials from the shift in energy of these accelerated distribution functions (DFs) from the source electron spectrum. We assume the source electron spectrum to be the least accelerated spectrum (associated with magnetic flux tubes not connected to the potential layer), which we obtain by averaging over distributions within the time range marked by two magenta vertical lines in Figure 1b6. The power law decrease at high energies is similar for the blue spectra and the source spectrum, suggesting these electrons share the same source but are shifted by a range of potentials. The energy shift from the source spectrum to the most accelerated blue spectrum is ~ 440 eV for both Period 1 (11:05:48–11:06:05 UT,

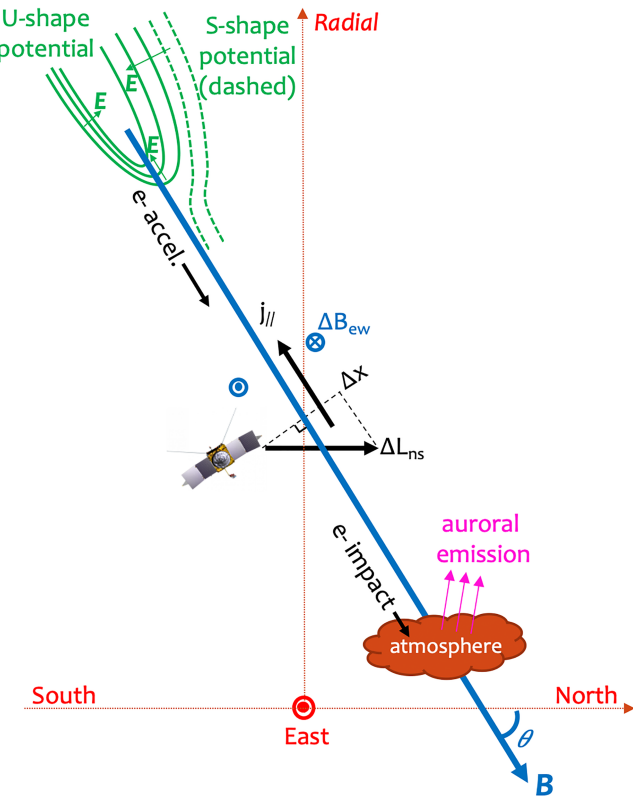


Figure 3. A schematic shows the geometry of the magnetic field, the field-aligned current, and the spacecraft motion in the local geographic frame, as well as the U- and/or S-shape potential structure and auroral emission by electron impact. The current sheet is perpendicular to the page with its projection the same as the magnetic field line, and the current within is antiparallel to the magnetic field. $\Delta x = \Delta L_{ns} \sin \theta$ is the distance perpendicularly across the magnetic field, as the spacecraft moved horizontally from south to north (ΔL_{ns}), and θ is the magnetic elevation angle.

(~50 km). In other words, assuming this current structure to be stable for this 10-s time period, the current sheet is perpendicular to the page with its projection the same as the magnetic field line, and the current within is antiparallel to the magnetic field. The spacecraft was crossing this current sheet at an angle equivalent to the magnetic elevation angle (θ) as the spacecraft moved horizontally from south to north instead of traversing the current sheet. This current sheet gave rise to a perturbation in magnetic field mostly in the east-west direction (ΔB_{ew}). Therefore, $j_{||} = \frac{1}{\mu_0} \frac{\Delta B_{ew}}{\Delta x} = \frac{1}{\mu_0} \frac{\Delta B_{ew}}{\Delta L_{ns} \sin \theta}$, where $\Delta x = \Delta L_{ns} \sin \theta$ is the distance perpendicularly across the magnetic field and $\theta = -60^\circ$ for this time period. The calculated field-aligned current density is displayed in Figure 1b3 as the blue curve, with a maximum magnitude of $\max(|j_{||}|) = 1.1 \mu\text{A/m}^2$, which is of the same order as terrestrial auroral currents. The field-aligned current $j_{||}$ is negative with respect to the radially inward magnetic field (Figure 1b1), and thus upward, consistent with downward traveling electrons being the main current carrier.

Similarly, for Period 2, the perturbation in magnetic field is mainly in the north-south direction but spreads over a larger spatial distance, which means the field-aligned current density is smaller than Period 1. These differences between Periods 1 and 2 might be explained by the spacecraft passing through different parts of the same potential/current structure or temporal variation of these structures. It is worth noticing that the background magnetic field is less clear for this period, and therefore, we carry out our quantitative calculation for Period 1 only.

These downward field-aligned currents are carried predominantly by electrons because of their high mobility, mainly precipitating superthermal (solar wind origin) electrons above the potential layer. We estimate the net current density carried by superthermal electrons (the red line in Figure 1b4) by integrating the

Figure 2a) and Period 2 (11:06:28–11:06:48 UT, Figure 2b). In other words, the field-aligned potentials can be up to ~440 V, or more if the spacecraft did not pass through field lines that sample the entire potential layer. The magnitude of this potential drop is similar to results based on observations from other Mars orbiters (e.g., Brain et al., 2006; Lillis et al., 2018; Lundin et al., 2007).

These accelerated blue DFs in Figures 2a and 2b match up with the source electron spectrum down to 20 eV or higher energies but not very low energies. Correspondingly, the source electrons have an isotropic distribution for PAs 0–180° below 20 eV but a loss cone above, as shown in Figure 2c. It is probable that this source electron spectrum experienced an acceleration around 20 V, and it is mainly secondary electrons below 20 eV.

4. Current Estimation

In this section, we evaluate whether the potential formation is similar to what occurs at Earth: Somewhere above the spacecraft, the ambient plasma cannot support an imposed field-aligned current, so that a potential forms to accelerate electrons to carry the current. To investigate this, we estimate field-aligned currents from magnetic field perturbations and then compare them to the net electron current.

To estimate currents from \mathbf{B} , we take the time period of 11:05:45–11:05:55 UT as an example, as highlighted by the black bar in Figure 1b2, during which the perturbation in magnetic field is mainly in the local east-west direction (ΔB_{ew}) and has a clear baseline or background field of −1.7 nT. We thus estimate the maximum magnetic disturbance of 4.2 nT in the east-west direction from a current layer by subtracting this background field of −1.7 nT. Over the same time interval, the spacecraft moved mainly horizontally from south to north, which gives a length scale in the north-south direction of $\Delta L_{ns} \sim -3.8$ km with a negligible radial motion $\Delta r \sim -0.5$ km. We can then simplify the geometry to what is shown in Figure 3 in the local geographic frame as it is a small-scale structure

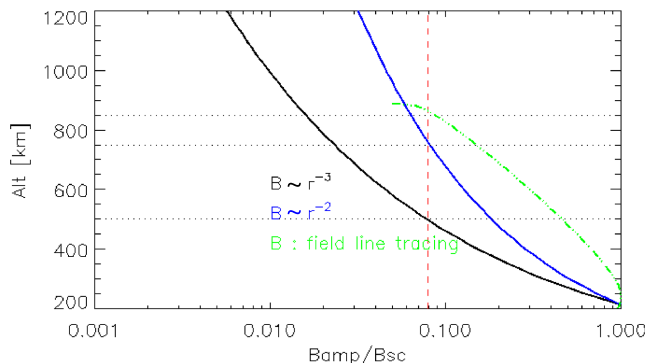


Figure 4. The ratio of the presumed magnetic field strength and the magnetic field strength at the spacecraft (Bsc) as a function of altitude. The black and blue lines assume the magnetic field amplitude vary as a function of r^{-3} and r^{-2} , respectively, where r is the distance from the dipole source and effectively the distance from the surface here. The green line is the profile based on magnetic field line tracing from a crustal field model (Morschhauser et al., 2014) starting at the spacecraft location at around 11:05:50 UT. The vertical red dashed line marks the critical ratio of ~ 0.08 .

DF for PA $0\text{--}60^\circ$ (downgoing) subtracted from that for PA $120\text{--}180^\circ$ (upgoing). The current density of these accelerated electrons has a maximum value of $\max(|j_{se}|) = 2.5 \mu\text{A/m}^2$ for Period 1, agreeing reasonably well with the maximum current density derived from the magnetic perturbation ($\max(|j_{||}|) = 1.1 \mu\text{A/m}^2$). The factor of two difference is probably because the spacecraft crossed the current sheet at an angle (i.e., the current sheet is rotated in the north-south direction from the east-west direction in the horizontal plane) or did not cross the center of the current sheet so that we underestimate the maximum field-aligned current density. Similarly, for Period 2, the maximum electron current density reaches $0.5 \mu\text{A/m}^2$, corresponding to a smaller current density from magnetic disturbances. In other words, the net current carried by the acceleration superthermal electrons agrees with the field-aligned current inferred from the observed magnetic perturbation.

Moreover, source electrons (Figure 2c) can be identified from SWEA observations, which give a net electron current $< 1 \times 10^{-2} \mu\text{A/m}^2$ (Figure 1b4), much smaller than the field-aligned current from ΔB . This suggests that the source electrons cannot carry the imposed current unless they are accelerated by an electrostatic potential.

5. Discussion of the Potential Layer

We can estimate the lower altitude limit of the potential layer with PA distributions of the source electrons and accelerated electrons. As shown in Figure 2c, the precipitating source electrons are observed to be isotropic for PA $0\text{--}90^\circ$. At high altitudes, isotropic source electrons become more field-aligned immediately after acceleration by the potential layer. As these now more beamed electrons travel to lower altitudes, the crustal magnetic field gets stronger and electron distributions broaden again in PA to conserve the first adiabatic invariant. These accelerated electrons are observed to be nearly isotropic again at the spacecraft for PA $0\text{--}90^\circ$ for energies above 100 eV (e.g., P-1 and P-2 in Figure 1b5), which establishes a minimum ratio of the magnetic field strength at the potential layer to that at the spacecraft.

Assume that, just above the potential layer, electrons have an energy ε_0 and an isotropic distribution for PA $0\text{--}90^\circ$ and a local magnetic field strength B_0 . After an acceleration of ϕ by the potential layer, these electrons have a width of PA of $\theta = \sin^{-1}(\sqrt{\varepsilon_0}/(\varepsilon_0 + e\phi))$ immediately below the potential layer. At a critical altitude with a magnetic field strength of B_C , the PA width becomes 90° , which means $B_0/B_C = \sin^2\theta = \varepsilon_0/(\varepsilon_0 + e\phi)$. This critical altitude has to be above the spacecraft so that $B_{SC} > B_C$, which gives $B_0/B_{SC} < \varepsilon_0/(\varepsilon_0 + e\phi)$, where B_{SC} is the magnetic field strength at the spacecraft. To estimate the lower altitude limit of the potential layer, given $\phi = 440$ V, we take the minimum ε_0 to be the temperature of the source electrons. By fitting the source distribution with a Gaussian distribution for 40–100 eV (as shown in supporting information Figure S1), we obtain $T_e = 37$ eV and $n_e = 0.44 \text{ cm}^{-3}$, which gives $B_0/B_{SC} < 0.08$. Figure 4 shows the ratio of the presumed magnetic field strength and B_{SC} against altitude for different approximations of the magnetic field configuration, $B \sim r^{-3}$ for a magnetic dipole (black), $B \sim r^{-2}$ for a line dipole (blue), and field tracing results from a crustal field model (Morschhauser et al., 2014) (green). The distance of the spacecraft from the crustal magnetic sources (~ 200 km) is small compared with the east-west extent of the crustal sources ($> 2,000$ km), so the latter two are better approximations. With the vertical red line marking the ratio of 0.08, we estimate the lower altitude limit for the potential layer to be around 750–850 km.

We can also estimate the magnitude of the associated field-aligned electric field. Assuming that the acceleration of these electrons comes from one double layer, then one can estimate the maximum parallel electric field associated with the acceleration. The thickness of a double layer at Earth is often ~ 10 Debye lengths (Andersson et al., 2002). As thermal plasma from below does not have sufficient energy to diffuse past the potential layer, we estimate the Debye length (λ_D) at the potential layer with the hot population, that is, the source electrons, which is ~ 70 m. Therefore, assuming the thickness to be $10\lambda_D$, given a total potential drop of 440 V, we can obtain a parallel electric field of ~ 0.6 V/m, similar to typical values at Earth.

The location of the potential layer can also be inferred from a statistical analysis of many electron acceleration events. Generally, field-aligned accelerated electrons are observed below the potential layer so that the

altitude distribution of these accelerated electrons can establish a lower altitude limit for the potential layer. Brain et al. (2006) reported tens of thousands of peaked spectra from MGS observations, which were made at a fixed altitude of ~ 400 km and fixed local times of 2 a.m./p.m. This suggests that many of the potential layers, assuming these are what caused the peaked spectra, occurred above 400-km altitude. Alternatively, field-aligned potentials can be inferred from the energy dependence of loss cone sizes, as well as accelerated ion beams, above the potential layer (e.g., Lundin et al., 1987, 2007; McFadden et al., 1998). It is reasonable to assume some of large field-aligned potentials derived from loss cone shapes with MGS data by Lillis et al. (2018) can be explained by the mechanism discussed here, which means potential layers might occur below 400 km as well.

6. Concluding Remarks

In this study, we analyze an electron acceleration event on 26 February 2019, closely associated in time and space with localized auroral emissions detected by the IUVS instrument. We infer the field-aligned potentials to be up to ~ 440 V from electron observations. At the edges of the most intense electron acceleration, significant magnetic perturbations were observed, which suggest the existence of a field-aligned current sheet. We estimate a maximum upward current density of $\max(|j_{\parallel}|) \sim 1.1 \mu\text{A}/\text{m}^2$. Meanwhile, the electron current carried by the identified source electrons is much smaller than $\max(|j_{\parallel}|)$, but that carried by the accelerated electrons can be up to $2.5 \mu\text{A}/\text{m}^2$ in locations where magnetic perturbations were observed. This set of observations suggests a mechanism very similar to what occurs at Earth: There exists a shear in magnetic fields at the open-closed field line boundary or a twist in magnetic fields, indicating a field-aligned current; when this current cannot be sustained by ambient plasma, a parallel electric field is needed. The potential acceleration gives the inverted-V electron signature.

We estimate that the lower altitude limit of the potential layer is around 750–850 km from the PA distributions of the source electrons and accelerated electrons. As the thickness of the potential layer is typically a few Debye lengths, we obtain $\lambda_D = 70$ m, and the associated parallel electric field is therefore estimated to be ~ 0.6 V/m.

Finally, we have manually searched for and identified inverted-V electron events from late February to March 2019 for when auroras were observed and found that these events mainly occurred near the terminator and over the strong crustal magnetic fields. This is consistent with MGS observations (e.g., Brain et al., 2006) of a clustering of inverted-V events near the strong crustal regions. This might suggest the importance of a significant intrinsic field, like Earth, for such a mechanism to operate. A more systematic statistical analysis is, however, needed to characterize the general behavior of these events.

Acknowledgments

This work was supported by the National Aeronautics and Space Administration (NASA) Grant NNN10CC04C to the University of Colorado and by subcontract to Space Sciences Laboratory, University of California, Berkeley. The MAVEN project is supported by NASA through the Mars Exploration Program. The MAVEN data used in this study are available through the Planetary Data System (<https://pds-ppi.igpp.ucla.edu/mission/MAVEN>). Parts of this work for the observations obtained with the SWEA instrument are supported by the French space agency CNES.

References

- Akbari, H., Andersson, L., Fowler, C., & Mitchell, D. (2019). Spectral analysis of accelerated electron populations at Mars. *Journal of Geophysical Research: Space Physics*, 124, 8056–8065. <https://doi.org/10.1029/2019JA026738>
- Andersson, L., Ergun, R., Newman, D., McFadden, J., Carlson, C., & Su, Y.-J. (2002). Characteristics of parallel electric fields in the downward current region of the aurora. *Physics of Plasmas*, 9(8), 3600–3609.
- Bertaux, J.-L., Leblanc, F., Witasse, O., Quemerais, E., Liliensten, J., Stern, S., et al. (2005). Discovery of an aurora on Mars. *Nature*, 435(7043), 790–794.
- Birn, J., Artemyev, A., Baker, D., Echim, M., Hoshino, M., & Zelenyi, L. (2012). Particle acceleration in the magnetotail and aurora. *Space Science Reviews*, 173(1–4), 49–102.
- Brain, D., Halekas, J., Peticolas, L., Lin, R., Luhmann, J., Mitchell, D., et al. (2006). On the origin of aurora on Mars. *Geophys. Res. Lett.*, 33, L01201. <https://doi.org/10.1029/2005GL024782>
- Brain, D., Lillis, R., Mitchell, D., Halekas, J., & Lin, R. (2007). Electron pitch angle distributions as indicators of magnetic field topology near Mars. *Journal of Geophysical Research*, 112, A09201. <https://doi.org/10.1029/2007JA012435>
- Connerney, J., Espley, J., Lawton, P., Murphy, S., Odom, J., Oliversen, R., & Sheppard, D. (2015). The MAVEN magnetic field investigation. *Space Science Reviews*, 195(1–35), 257–291.
- Deighan, J., Jain, S., Chaffin, M., Fang, X., Halekas, J., Clarke, J., et al. (2018). Discovery of a proton aurora at Mars. *Nature Astronomy*, 2(10), 802.
- Ergun, R., Andersson, L., Main, D., Su, Y.-J., Newman, D., Goldman, M., et al. (2004). Auroral particle acceleration by strong double layers: The upward current region. *Journal of Geophysical Research*, 109, A12220. <https://doi.org/10.1029/2004JA010545>
- Evans, D. S. (1974). Precipitating electron fluxes formed by a magnetic field aligned potential difference. *Journal of Geophysical Research*, 79(19), 2853–2858.
- Feldman, W., Anderson, R., Bame, S., Gary, S., Gosling, J., McComas, D., et al. (1983). Electron velocity distributions near the Earth's bow shock. *Journal of Geophysical Research*, 88(A1), 96–110.
- Haerendel, G., Frey, H., Bauer, O., Rieger, E., Clemons, J., Boehm, M., et al. (1994). Inverted-V events simultaneously observed with the Freja satellite and from the ground. *Geophysical Research Letters*, 21(17), 1891–1894.

- Jakosky, B. M., Lin, R., Grebowsky, J., Luhmann, J., Mitchell, D., Beutelschies, G., et al. (2015). The Mars Atmosphere and Volatile Evolution (MAVEN) mission. *Space Science Reviews*, 195(1-4), 3–48.
- Leblanc, F., Witasse, O., Liljensten, J., Fahrm, R. A., Safaeenili, A., Brain, D. A., et al. (2008). Observations of aurorae by SPICAM ultraviolet spectrograph on board Mars Express: Simultaneous ASPERA-3 and MARSIS measurements. *Journal of Geophysical Research*, 113, A08311. <https://doi.org/10.1029/2008JA013033>
- Leblanc, F., Witasse, O., Winningham, J., Brain, D., Liljensten, J., Blelly, P.-L., et al. (2006). Origins of the Martian aurora observed by Spectroscopy for Investigation of Characteristics of the Atmosphere of Mars (SPICAM) on board Mars Express. *Journal of Geophysical Research*, 111, A09313. <https://doi.org/10.1029/2006JA011763>
- Liemohn, M. W., Ma, Y., Nagy, A., Kozyra, J., Winningham, J., Fahrm, R., et al. (2007). Numerical modeling of the magnetic topology near Mars auroral observations. *Geophysical Research Letters*, 34, L24202. <https://doi.org/10.1029/2007GL031806>
- Lillis, R. J., & Brain, D. A. (2013). Nightside electron precipitation at Mars: Geographic variability and dependence on solar wind conditions. *Journal of Geophysical Research: Space Physics*, 118, 3546–3556. <https://doi.org/10.1002/jgra.50171>
- Lillis, R. J., Halekas, J., Fillingim, M., Poppe, A., Collinson, G., Brain, D. A., & Mitchell, D. (2018). Field-aligned electrostatic potentials above the Martian exobase from MGS electron reflectometry: Structure and variability. *Journal of Geophysical Research: Planets*, 123, 67–92. <https://doi.org/10.1002/2017JE005395>
- Lundin, R., Eliasson, L., Hultqvist, B., & Stasiewicz, K. (1987). Plasma energization on auroral field lines as observed by the Viking spacecraft. *Geophysical Research Letters*, 14(4), 443–446.
- Lundin, R., Winningham, D., Barabash, S., Fahrm, R., Brain, D., Nilsson, H., et al. (2007). Auroral plasma acceleration above Martian magnetic anomalies, *The Mars plasma environment* (pp. 333–354). New York, NY: Springer.
- Marklund, G., Johansson, T., Lile, S., & Karlsson, T. (2007). Cluster observations of an auroral potential and associated field-aligned current reconfiguration during thinning of the plasma sheet boundary layer. *Journal of Geophysical Research*, 112, A01208. <https://doi.org/10.1029/2006JA011804>
- Mauk, B. H., Haggerty, D., Paranicas, C., Clark, G., Kollmann, P., Rymer, A., et al. (2017). Discrete and broadband electron acceleration in Jupiter's powerful aurora. *Nature*, 549(7670), 66.
- McClintock, W. E., Schneider, N. M., Holsclaw, G. M., Clarke, J. T., Hoskins, A. C., Stewart, I., et al. (2015). The Imaging Ultraviolet Spectrograph (IUVS) for the MAVEN mission. *Space Science Reviews*, 195(1-4), 75–124.
- McFadden, J., Carlson, C., & Boehm, M. (1986). Field-aligned electron precipitation at the edge of an arc. *Journal of Geophysical Research*, 91(A2), 1723–1730.
- McFadden, J., Carlson, C., Ergun, R., Mozer, F., Temerin, M., Peria, W., et al. (1998). Spatial structure and gradients of ion beams observed by FAST. *Geophysical Research Letters*, 25(12), 2021–2024.
- Mitchell, D., Mazelle, C., Sauvad, J.-A., Thocaven, J.-J., Rouzaud, J., Fedorov, A., et al. (2016). The MAVEN solar wind electron analyzer. *Space Science Reviews*, 200(1-4), 495–528.
- Morschhauser, A., Lesur, V., & Grott, M. (2014). A spherical harmonic model of the lithospheric magnetic field of Mars. *Journal of Geophysical Research: Planets*, 119, 1162–1188. <https://doi.org/10.1002/2013JE004555>
- Partamies, N., Donovan, E., & Knudsen, D. (2008). Statistical study of inverted-V structures in FAST data, *Annales Geophysicae* (Vol. 26, pp. 1439–1449). <https://doi.org/10.5194/angeo-26-1439-2008>
- Paschmann, G., Haaland, S., & Treumann, R. (Eds.). (2002). *Auroral plasma physics*. Norwell, Mass: Kluwer Acad.
- Ritter, B., Gérard, J.-C., Hubert, B., Rodriguez, L., & Montmessin, F. (2018). Observations of the proton aurora on Mars with SPICAM on board Mars Express. *Geophysical Research Letters*, 45, 612–619. <https://doi.org/10.1002/2017GL076235>
- Schneider, N. M., Deighan, J. I., Jain, S. K., Stiepen, A., Stewart, A. I. F., Larson, D., et al. (2015). Discovery of diffuse aurora on Mars. *Science*, 350(261), aad0313.
- Schneider, N. M., Jain, S. K., Deighan, J., Nasr, C. R., Brain, D. A., Larson, D., et al. (2018). Global aurora on Mars during the September 2017 space weather event. *Geophysical Research Letters*, 45, 7391–7398. <https://doi.org/10.1029/2018GL077772>
- Schwartz, S. J., Andersson, L., Xu, S., Mitchell, D. L., Akbari, H., Ergun, R. E., et al. (2019). Collisionless electron dynamics in the magnetosheath of Mars. *Geophysical Research Letters*, 46, 11,679–11,688. <https://doi.org/10.1029/2019GL085037>
- Steckiewicz, M., Garnier, P., André, N., Mitchell, D. L., Andersson, L., Penou, E., et al. (2017). Comparative study of the Martian suprathermal electron depletions based on Mars Global Surveyor, Mars Express, and Mars Atmosphere and Volatile Evolution mission observations. *Journal of Geophysical Research: Space Physics*, 122, 857–873. <https://doi.org/10.1002/2016JA023205>
- Steckiewicz, M., Mazelle, C., Garnier, P., André, N., Penou, E., Beth, A., et al. (2015). Altitude dependence of nightside Martian suprathermal electron depletions as revealed by MAVEN observations. *Geophysical Research Letters*, 42, 8877–8884. <https://doi.org/10.1002/2015GL065257>
- Weber, T., Brain, D., Mitchell, D., Xu, S., Connerney, J., & Halekas, J. (2017). Characterization of low-altitude nightside Martian magnetic topology using electron pitch angle distributions. *Journal of Geophysical Research: Space Physics*, 122, 9777–9789. <https://doi.org/10.1002/2017JA024491>
- Weber, T., Brain, D., Mitchell, D., Xu, S., Espley, J., Halekas, J., et al. (2019). The influence of solar wind pressure on Martian crustal magnetic field topology. *Geophysical Research Letters*, 46, 2347–2354. <https://doi.org/10.1029/2019GL081913>
- Xu, S., Mitchell, D., Liemohn, M., Fang, X., Ma, Y., Luhmann, J., et al. (2017). Martian low-altitude magnetic topology deduced from MAVEN/SWEA observations. *Journal of Geophysical Research: Space Physics*, 122, 1831–1852. <https://doi.org/10.1002/2016JA023467>